Cite this: DOI: 00.0000/xxxxxxxxxx

Lattice dynamics of $Ge_{1-x}Sn_x$ alloy nanowires†

Sreyan Raha,[a] Subhajit Biswas,[b] Jessica Doherty,[b] Prasanna Kumar Mondal,[c] Justin D. Holmes, [b] and Achintya Singha[a*]

Received Date
Accepted Date

DOI: 00.0000/xxxxxxxxxx

Alloying group IV semiconductors offers an effective way to engineer their electronic properties and lattice dynamics. The incorporation of Sn in Ge permits a transition from an indirect to a direct bandgap semiconductor. Here, by combining polarization, laser power-dependent and temperature-dependent micro-Raman spectroscopy we explore the full lattice dynamics of $Ge_{1-x}Sn_x$ (x= 0.01, 0.06 and 0.08) alloy nanowires. In the high Sn content samples ($x \geq 0.06$), a low-frequency tail and a high-frequency shoulder are observed which are associated with the F_{2g} optical phonon mode of Ge (Ge–Ge mode). The new modes are assigned to the stretching of Ge–Ge bonds due to Sn-induced lattice relaxation and compression, respectively. The symmetry of the observed Raman modes has been studied by polarization-dependent Raman scattering. Nonlinear fitting of the laser power-dependent intensity of the highfrequency Ge–Ge mode in the $Ge_{1-x}Sn_x$ alloy nanowires with x = 0.06 and 0.08 suggests the activation of a third-order stimulated Raman scattering process, due to the high intensity localized electric field surrounding the Sn clusters. Finally, from the temperature-dependent Raman study, we have estimated the isobaric Grüneisen parameters for all the observed modes.

1 Introduction

Germanium (Ge) is a promising group IV material for both photonic and electronic applications.The poor light emission properties due to the indirect bandgap of Ge can be overcome by various approaches such as doping, strain and crystal structure modification as the gap between indirect (L) and direct(G) conduction band valley of Ge is small (140 meV) [1–3]. Among the different methods, alloying with Sn have shown promising performance and required extensive research efforts. Recently, the direct bandgap has been realized in Ge nanowire by Sn incorporation [4,5].These direct band gap group IV alloys are emerging class of materials for fundamental studies as well as novel technological applications such as tunnel FETs [6], optical interconnects [7] and group IV photonics [7,7,8,8–20]. In addition to the direct band to band transition of carriers, group IV alloy systems (e.g. GeSn) have also been predicted to exhibit low carrier effective masses and high electron and hole mobilities, which make them ideal materials for application in optoelectronic and high speed electronic devices [21].

However, doping and alloying may cause defect induced lattice imperfection due to lattice parameter mismatch [22].Defects in semiconductors may lead to many unique phenomena such as weak localization, appearance of new vibrational modes, electron-phonon interaction etc. [22–29].The optical and electronic phenomena of semiconducting materials are well known to be influenced by the basic interactions of doping elements with lattice vibrations [22,29,30].Thus, an understanding of lattice dynamics is crucial for manipulating the optical and electronic properties of semiconductor materials. Reliable fabrication of high-quality alloy nanostructures such as quantum wells and nanowires (NWs) depends in part on the availability of rapid, contactless and non-destructive characterization techniques to ascertain composition and crystal quality, and to assess the alloy microstructure. Raman spectroscopy is one of the most used non-destructive tools to detect the signature of the phonon modes and their nature in nanostructured materials.

In this work, we present the lattice dynamics of $Ge_{1-x}Sn_x$ alloy NWs using micro-Raman spectroscopy. We uncover the composition dependent shift of phonon modes and their origin. The symmetry of the modes is explored by the polarization-dependent measurements. In the NWs with high Sn concentration, the Sn induced stimulated Raman scattering (SRS) has been probed by a laser power-dependent Raman study. Finally, insight into the temperature dependent phonon dynamics is reported.

2 Methodology

$Ge_{1-x}Sn_x$ NWs were grown using a liquid-injection chemical vapour deposition (LICVD) technique [4,31,32]. Using previously reported synthesis method (for detailed synthesis method see Ref. [4]), $Ge_{1-x}Sn_x$ NWs were grown on Si (001) substrates with diphenyl germane (DPG) as Ge and allyltributyl stanane (ATBS) as Sn precursor respectively. Synthesis was performed at 440 °C with Au and AuAg (90:10) nanoparticles as catalysts. Three $Ge_{1-x}Sn_x$ (x= 0.01, 0.06 and 0.08) NW samples with varied Sn incorporation were obtained by varying the concentrations of ATBS in the precursor solution.

$Ge_{1-x}Sn_x$ NWs were imaged on a FEI Helios Nanolab 600i for scanning electron microscopy (SEM) and Nion UltraSTEM100 mi-

[a] Department of Physics, Bose Institute, 93/1 Acharya Prafulla Chandra Road, Kolkata 700009
* achintya@jcbose.ac.in
[b] School of Chemistry & Advanced Materials and Bioengineering Research (AMBER) Centre, University College Cork, Cork T12 YN60, Ireland
[c] Department of Physics, Surendranath College, Kolkata 700009, India
† Electronic Supplementary Information (ESI) available. See DOI: 00.0000/00000000.

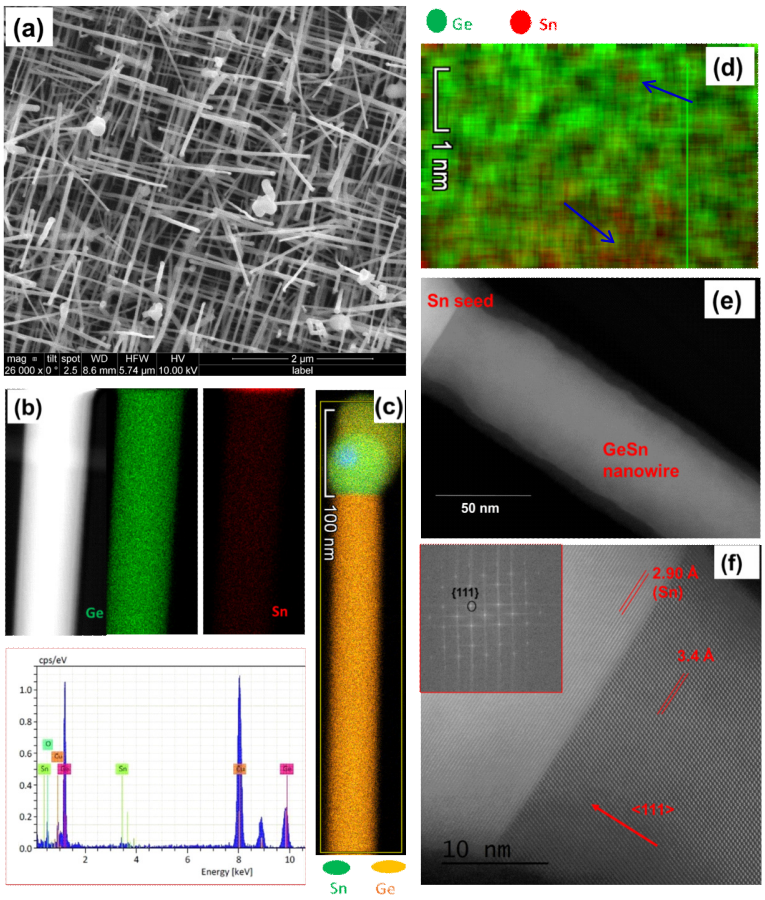

Fig. 1 (a) SEM image of a representative $Ge_{1x}Sn_x$ (x = 0.08) nanowire sample. (b)–(d) Elemental analysis of the NWs. Elemental maps (and the corresponding HAADF image) in parts. (b) and (c) Show the presence of Sn in the tip of a NW, with the nanowire body mainly comprising Ge with a small amount (8 at %) of Sn. The attached EDX spectrum of the NW part confirms the presence of Sn in the NW. A high-resolution elemental map of the NW lattice is shown in part (d). (e) and (f) are STEM analysis of the NWs. Part (e) shows a single NW with a bright contrasted Sn catalyst at the tip. A high resolution image from the same nanowire of the area near the seed–nanowire interface can be seen in part (f), showing a highly crystalline structure. The NWs are <111> oriented, as determined by FFT analysis (inset, red box). There is a sharp interface between the seed and the body of the NW.

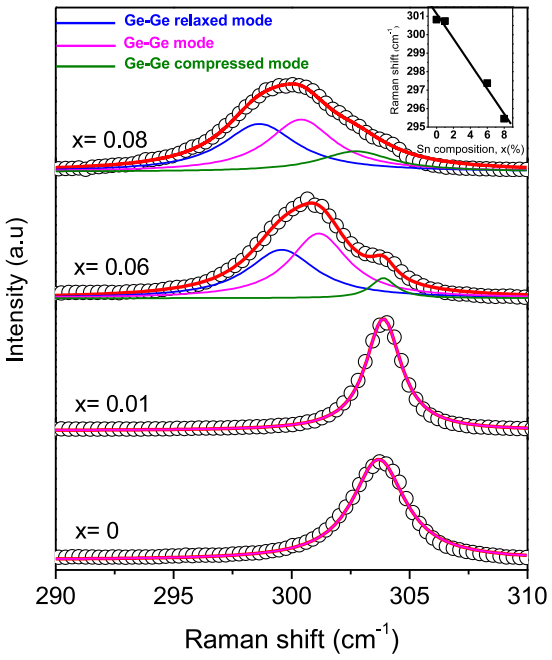

Fig. 2 Deconvoluted Raman spectra measured at 83 K for $Ge_{1x}Sn_x$ NWs with x = 0 to 0.08 as labelled in the figure. Discrete points are experimental data and red solid curves are the fitted spectra, while magenta, blue and green solid curves represent the F2g (Ge–Ge mode), Ge–Ge relaxed and Ge–Ge compressed modes, respectively. The inset shows the Sn concentration dependent Raman shift where experimental points are represented by black squares and the line shows the fitted curve.

croscope operated at 100 kV for high-resolution scanning transmission electron microscopy (HRSTEM). Energy dispersive x-ray analysis (EDX) mapping was performed using a Titan Themis double-corrected and monochromated TEM at 300 kV. Probe-forming optics were adjusted to deliver a 80 pm probe, with 40 pA beam current and 27 mrad convergence semi-angle. Raman scattering was performed in a LabRAM HR microRaman spectrometer equipped with 1800 lines per mm grating and a peltier cooled CCD detector. An air cooled Argon-ion laser of wavelength 488 nm was used as excitation light source, and a 100× objective with numerical aperture (NA) of 0.9 was used to focus the laser on the sample and to collect data from the sample. Polarization control was realized by a set of linear polarizer and half wave plate. Temperature dependent measurement was performed using a Linkam THMS600.

3 Results

Figure 1(a) shows the representative SEM image of $Ge_{1-x}Sn_x$ (x= 0.08) NWs. SEM image shows uniform NW morphology with the negligible presence of spherical clusters in the sample, representative of all $Ge_{1-x}Sn_x$ NW samples (x= 0.01-0.08) grown via the bottom-up method. NW diameters were are around 40-60 nm, whereas the length of the NW mostly varied between 1-2 μm. Mean Sn concentrations in the NWs, as determined via EDX point analysis (calculated from 50 NWs), were x= 1 , 6 and 8 at.% for three different NW samples. EDX maps from the bulk of the NWs confirmed the homogenous distribution of Sn in body of the NWs [Figure 1(b)]. A representative EDX spectra is shown in this part of the figure. Sn rich spherical nanoparticle catalyst seeds at tips of the NWs was also confirmed from EDX map analysis [Figure 1(c)]. The presence of Sn at NW tip justifies the participation of a vapour-liquid-solid growth method with in-situ formed Sn-rich seed for the $Ge_{1-x}Sn_x$ nanowire growth. However, an ultra high-resolution EDX map of the $Ge_{1-x}Sn_x$ NW depicts the formation of small Sn clusters [shown by blue arrow in Figure 1(d)] within the Ge lattice.

Figure 1 (e) and (f) shows a representative high-angle annular-dark-field (HAADF) scanning transmission electron microscope (STEM) image and corresponding high-resolution image for $Ge_{1-x}Sn_x$ NW with 8 at. % Sn. Nanowires with 1 and 6 at. % Sn concentrations displayed similar structural qualities. High-resolution STEM image [Figure 1(f)] revealed the highly crystalline nature of the NWs. For all three NW samples, no crystal defects such as stacking faults and twinning were observed. HAADF-STEM from the crystalline $Ge_{1-x}Sn_x$ NWs revealed an interplanar spacing *(d)* of 0.34 nm [Figure 1 (f)], which is marginally larger than the *d* value for bulk diamond Ge crystals of 0.326 nm (JCPDS 04–0545), corresponding to (111) planes of Ge diamond cubic crystal structure. The recorded Fast Fourier Transform (FFT) pattern (inset of Figure 1f) corresponds to cubic Ge and the spot pattern indicates that the $Ge_{1-x}Sn_x$ NWs are single-crystalline. FFT showed a pseudohexagonal symmetry and the NW growth direction can be assigned along <111>, commonly observed growth direction for all the NWs.

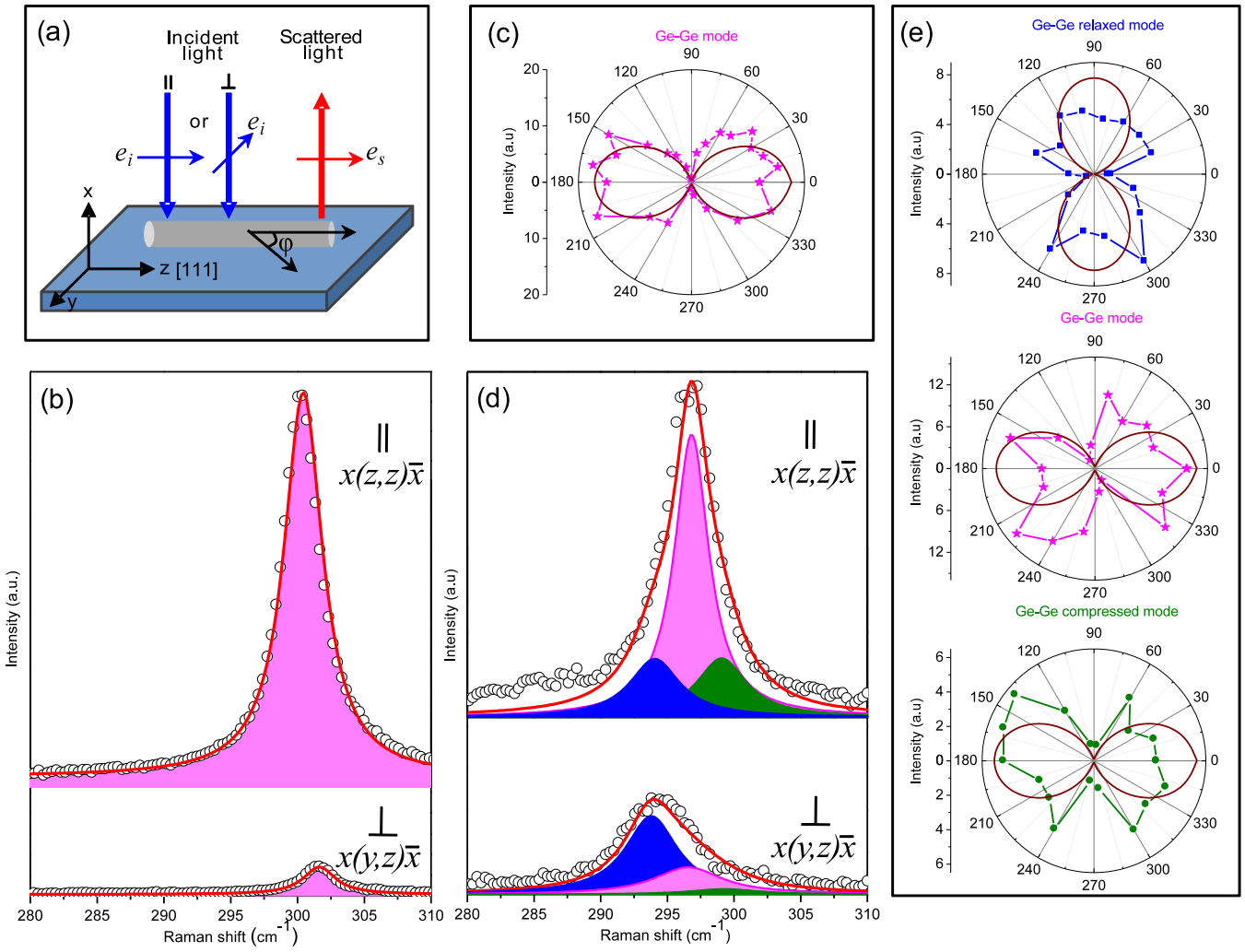

Fig. 3 (a) Illustration of the scattering geometry for polarized Raman measurements on a $Ge_{1-x}Sn_x$ NW. The co-ordinate system is chosen according to the geometry and crystal structure of the NW. The incident and scattered light propagate along the x and $\bar{x}$ axis and their polarization e_i and e_s lie in the yz plane. (b) Raman spectrum [discrete points are experimental data while red solid curve represents fitted spectrum] of a pure Ge NW when e_i and e_s are parallel (upper spectrum) and perpendicular(lower spectrum), (c) Polarized 360^o response of F_{2g} of an individual pure Ge NW. The solid brown curve represents the fit to the experimental data using $I \propto cos^2\phi$, (d) Raman spectrum [discrete points are experimental data while brown solid curve represents fitted spectrum] of a $Ge_{1-x}Sn_x$ NW with 6 at. % Sn when e_i and e_s are in a parallel (upper spectrum) and perpendicular (lower spectrum) polarization configuration. (e) Polarized 360^o response of all Raman components of an individual $Ge_{1-x}Sn_x$ NW with 6 at. % Sn. The solid brown curves represent the fit to the experimental data using $I \propto sin^2\phi$ for Ge-Ge relaxed mode and $I \propto cos^2\phi$ for F_{2g} and Ge-Ge compressed mode.

Figure 2 shows representative Raman spectra collected from $Ge_{1-x}Sn_x$ alloy NWs (x=0 to 8 at. %) at 80 K. We carefully evaluated the Raman spectra and it can be categorized into two types. Pure Ge NWs and NWs with Sn concentration of 1 at. % which exhibit a Raman active F_{2g} mode associated with diamond cubic Ge (Ge-Ge mode) are observed at around 304 cm^{-1}. However Raman spectra of Ge alloy NWs containing 6 and 8 at. % Sn displayed broad and asymmetric peaks at around 304 cm^{-1}. A quantitative analysis of the measured spectra through the deconvolution of multiple Lorentzian curves allows us to identify the minimum number of spectral contribution needed to describe the experimental spectrum. The Ge-Ge mode, the low frequency asymmetric broadening and high frequency shoulder of the Ge-Ge mode are fitted with three Lorentzian functions as displayed in Figure 2. A composition dependent redshift of the F_{2g} mode with the increase of Sn concentration is shown in the inset of Figure 2. The data is fitted with a linear formula: $\omega = 304 - ax$ where a=62.4 $\pm$ 0.062 cm^{-1}. The value of a is consistent with previous studies[4,33]. Atomistic Raman spectra calculations in Ref.[34] demonstrate that the short range alloy disorder is responsible for the redshift. The global lattice expansion and softening of the elastic constants in response to Sn incorporation drive the overall Ge-Ge mode redshift and the alloy microstructure impact the spectral shape of the Ge-Ge mode peak. The distribution of relaxed Ge-Ge nearest-neighbor bond lengths in the alloy generates contributions to the Ge-Ge mode peak that are spread over a range of frequencies. Stretching of the majority of Ge-Ge bonds in the alloy acts to decrease individual bond optical vibrational frequencies, giving rise to a broad, asymmetric tail on the low-frequency side of the primary Ge-Ge mode Raman peak. Compression of Ge-Ge bonds in the alloy, arising due to the presence of nearby Sn-Sn nearest-neighbor pairs, larger Sn clusters and Ge-Sn complexes, acts to increase individual bond optical vibrational frequencies, and can give rise to a "shoulder" on the high-frequency side of the primary Ge-Ge mode peak. Thus, the modes in high Sn contained samples are assigned as a Ge-Ge relaxed mode, a Ge-Ge mode and a Ge-Ge compressed mode. A schematic presentation of the three vibrational modes of $Ge_{1-x}Sn_x$ NWs with x $\geq$ 0.06 is displayed in the supplementary material (see Figure S1).

3.1 Polarization-dependent Raman spectroscopy

To get information about the Raman selection rule, polarization-dependent Raman measurements were performed. The intensity of a Raman mode for polarization of incident (e_i) and scattered (e_s) photon is given by equation 1:

$$I = |\langle e_i|R|e_s\rangle|^2 \quad (1)$$

where R is the Raman susceptibility tensor which is unique for any given Raman band. Therefore, the dependency of intensity of a phonon mode on the incident or scattered photon polarization permit investigation of the symmetry of the crystal and Raman selection rules.

The measurement was carried out in backscattering configuration on a single NW and the geometry of the experimental configuration is shown in Figure 3(a). The coordinate system x, y, z was chosen in keeping with NW shape and the corresponding crystallographic directions. Light incident on the NW was along the x direction and scattering occurred along the $\bar{x}$-direction. The e_i and e_s lie in the yz plane. According to the Porto notation, the Raman spectra obtained are labelled as $x(z,z)\bar{x}$ when e_i and e_s both are along the z-direction (parallel configuration) and as $x(y,z)\bar{x}$ when e_i is along the y direction but e_s is along the z direction (perpendicular configuration). The polarized Raman spectra of a pure Ge NW for both configurations are depicted in Figure 3(b). The significant drop in the intensity of the F_{2g} mode in cross polarization configuration compared to parallel configuration implies the high quality of the crystal[35]. Apart from the Raman selection rule, the light absorption and scattering by the NWs were highly sensitive to the polarization of the light, as the NW is a nanometer-sized antenna. We have measured the Raman intensity of the NW varying incident light polarization (ϕ) from 0 to 360^o and the result is displayed in Figure 3(c). In order to interpret the experimental data we have compared the result with calculated Raman intensity, $I \propto cos^2\phi$ obtained from equation (1) using a Raman tensor of F_{2g} mode of diamond cubic crystals[35]. The calculation is consistent with the experimental data as shown in Figure 3(c). We also estimated polarization degree (R_i) of the mode using equation 2[36]:

$$R_i = \frac{I_{i,max} - I_{i,min}}{I_{i,max} + I_{i,min}} \quad (2)$$

where $I_{i,max}$ and $I_{i,min}$ are the maximum and minimum intensity of the i_{th} mode respectively. Taking the value of $I_{i,max}$ and $I_{i,min}$ from the polarized 360^o response of Raman data the calculated value of R_i for F_{2g} mode of a pure Ge NW is 95%. The polarization-dependent Raman study on $Ge_{1-x}Sn_x$ alloy NW with 6 at. % Sn is presented in Figure 3(d). Similar to a pure Ge NW, a large reduction in the intensity of the F_{2g} mode was observed for scattering in the perpendicular configuration compared to the parallel configuration (magenta shaded curve). The Ge-Ge compressed mode (green shaded curve) shows the same polarization selection rule as F_{2g} whereas the Ge-Ge relaxed mode (blue curve) shows the opposite behavior. The polarization behaviour of the F_{2g} mode and the Ge-Ge relaxed mode is consistent with earlier work by G. Abstreiter's group[37] where they reported similar modes in Si/Ge as LO and TO vibrations. A full angular dependent polar response of the F_{2g} and Ge-Ge compressed mode intensities are $\propto cos^2\phi$ but the Ge-Ge relaxed mode intensity is $\propto sin^2\phi$ (red solid curves in Figure 4(e)). The R_i values for F_{2g}, Ge-Ge compressed and Ge-Ge relaxed modes are 0.58, 0.73 and 0.72. A large change of polarization degree of the F_{2g} mode in $Ge_{1-x}Sn_x$ NWs with 6 at. % Sn compared to the pure Ge NWs (95% to 58%) implies that the Sn related disorders relaxes the Raman selection rule.

3.2 Laser power-dependent Raman spectroscopy

To aid the experimental confirmation of the origin of the mode at the high frequency shoulder of F_{2g} mode, which is predicted as the compressed Ge-Ge mode, we have performed laser power dependent Raman measurement on the NWs in 0.02 mW to 2.30 mW regime. At each laser power, the intensity of the individual

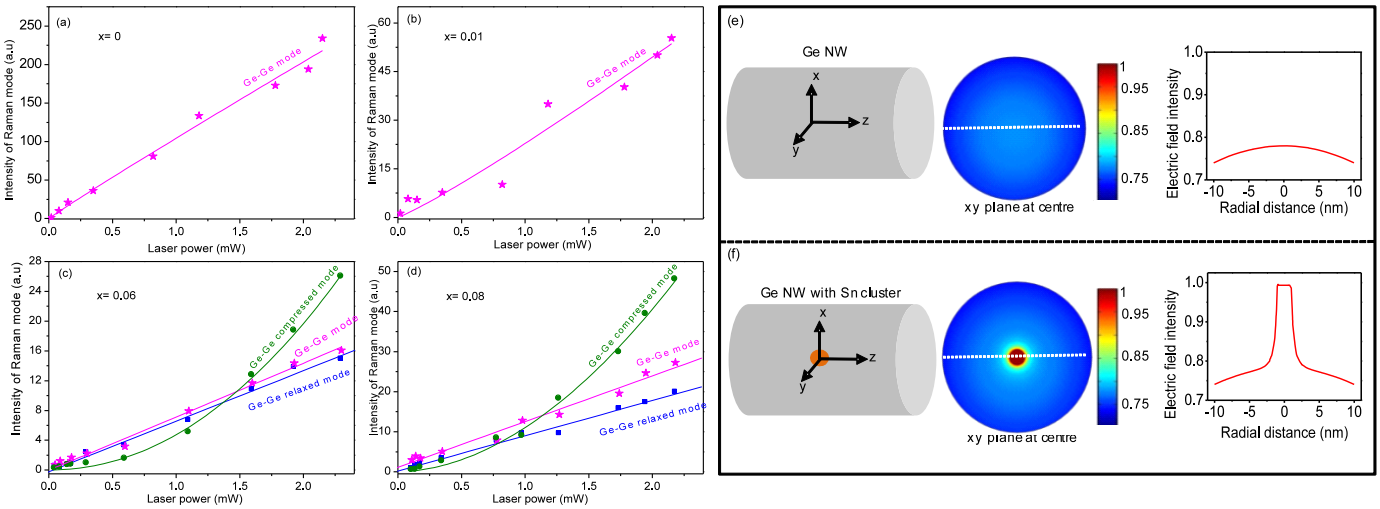

Fig. 4 Laser power dependency of the Raman modes intensities for (a) a pure Ge NW, and a $Ge_{1-x}Sn_x$ NW with (b) x= 0.01, (c) x= 0.06 and (d) x= 0.08. The discrete points are experimental data while the solid lines represent the fitting. Power-law fitting (green curve) for the high frequency mode in a $Ge_{1-x}Sn_x$ NW with x= 0.06 and x= 0.08 displaying a non-linear exponent of 2.1 and 1.9, respectively. Structures for simulation [left panel of Figure (e) & (f)] using COMSOL Multiphysics program. Cross sectional view (xy plane at $z = 0$) of calculated electric field [middle panel of Figure (e) & (f)]. Line profile of the calculated electric field (right panel) along the diameter of the cross sectional view of the electric field (white dotted line)

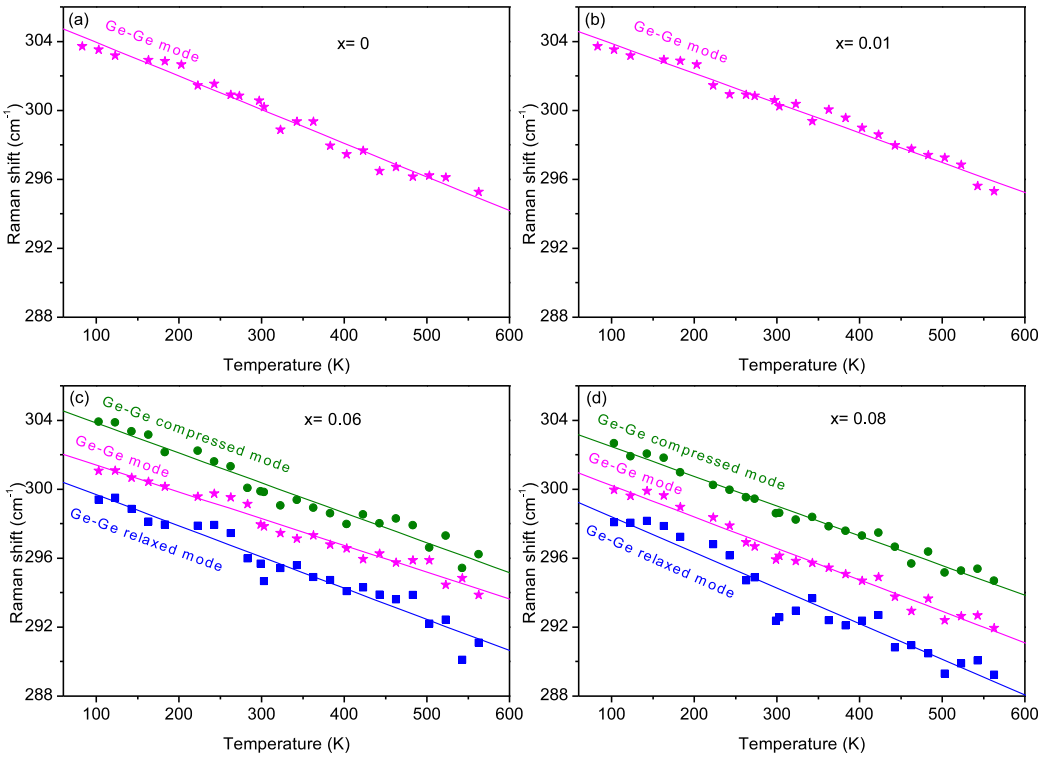

Fig. 5 Peak position of Ge-Ge mode,Ge-Ge relaxed mode and Ge-Ge compressed mode as a function of temperature for $Ge_{1-x}Sn_x$ NWs with (a) x= 0, (b) x = 0.01, (c) x = 0.06, (d) x = 0.08. Discrete points are the experimental data while solid curves represents the linear fitting using equation (3).

Raman mode of all the samples was estimated from the analysis of the data presented in the supplemental material (see Figure S2) and displayed in Figure 4(a-d). A power law fitting gives a linear exponent for all the modes except the high energy shoulder peak of $Ge_{1-x}Sn_x$ NW with 6 and 8 at. % Sn, which shows a non-linear exponent of 2.1 and 1.9, respectively. The non-linear behavior suggests the possible involvement of a third-order stimulated Raman scattering (SRS) process[38–40].

During Raman measurements, the continuous laser beam shining onto a Sn cluster can generate a highly enhanced excitation field at the close vicinity of its surface which gives rise to a broadband plasmonic emission. To verify this we have modeled electric field distribution inside a pure Ge NW and a Ge NW with a Sn cluster placed at its centre at a wavelength of 488 nm. The structure used in the COMSOL Multiphysics simulation is presented in the left panel of Figure 4(e & f). The cross sections (*xy* plane) of the calculated electric field distribution at $z = 0$ for both NWs are presented in the middle panel of Figure 4 (e & f).Very little of the electric field penetrates the NW but a plasmon induced localized electric field enhancement occurs at close vicinity to the Sn cluster. The electric field profile corresponding to the selected line (white dotted line) along the diameter of the field distribution in the *xy* plane is shown in the right panel of Figure 4 (e) & (f). The local field acts as a microscopic analogue to the Raman probe source used in the conventional SRS process and creates a plasmon induced non-linear Raman scattering in Ge NWs incorporating a high Sn. Here, an in-situ plasmonic probe source is generated by the Sn clusters which activates the stimulated (non-linear) Raman scattering process in the high-frequency Ge-Ge mode. Thus the laser power dependent Raman measurements highlights a correlation between Sn clusters and the Ge-Ge compressed mode, which confirms that the compression caused by the Sn clusters is the origin of the high frequency mode.

3.3 Temperature-dependent Raman spectroscopy

Thermodynamic properties, especially the knowledge of temperature dependent phonon behavior in new alloy semiconductor NWs such as GeSn NWs is important for their applications. Measuring the thermal parameters of nanostructured materials is very challenging. Temperature dependent Raman spectroscopy is a simple, convenient and contact less method for probing the thermal properties of 2D, as well as 1D nanostructures[42,43]. The temperature dependent Raman modes of $Ge_{1-x}Sn_x$ (x=0.01,0.06 and 0.08) alloy NWs were investigated over a temperature range between 83 to 523 K. Figure 5 shows the temperature dependent Raman modes of the NWs estimated from the temperature dependent Raman data presented in Figure S3 (see supplemental material). All the modes show a monotonic redshift with temperature, which can be attributed to the effect of thermal expansion and phonon-phonon interactions. This temperature dependent Raman shift was analyzed by using a linear approximation originated from model developed by Balkanski, as shown in equation 3[44].

$$\omega_T = \omega_0 + \beta T \tag{3}$$

where ω_o is the Raman frequency at 0 K and β is the first order temperature coefficient.

The higher order temperature coefficients are ruled out as they are not important in the temperature range investigated in this study. The slope of the fitted curve (solid lines in Figure 5) is the measure of the first order temperature coefficient, β, presented in the fourth column of the Table I.

An understanding of the anharmonicity and the temperature dependent thermo-mechanical properties of materials are of great importance for their technological development. The Grüneisen parameter, which connects phonon frequency and volume, can be taken as a convenient measure of anharmonicity of a crystal. The isobaric Grüneisen parameter (γ_p) describes as the change in the unit cell volume as a function of temperature. It relates the property of a material to its vibrational energy and indicates how anharmonic effects influence phonon spectrum under temperature. The γ_p for the i^{th} Raman mode(γ_{ip}) is related to β_i by the equation 4 given by:

$$\gamma_{ip} = -\frac{\beta_i}{\alpha\omega_i} \tag{4}$$

where, ω_i is the Raman frequency of i_{th} phonon mode, α is the thermal expansion coefficient. To calculate γ_{ip}, we have taken the value of α for Sn-Ge alloy system from Roucka et al[41]. Using equation (4), a complete set of γ_{ip} is reported in the last column of Table I. The estimated γ_{ip} value is lower for Ge NWs doped with 1 at.% Sn compared with pure Ge NWs and high Sn content samples. The result implies that $Ge_{1-x}Sn_x$ alloy NWs with x = 1 at. % potentially show better thermal transport behavior compared to the other samples, as thermal conductivity is inversely related to the γ_{ip}[45,46].

4 Conclusions

In summary, lattice dynamics of $Ge_{1-x}Sn_x$ alloy NWs were studied by Raman spectroscopy. The degenerate F_{2g} mode of diamond cubic Ge is red-shifted and broadened due to Sn incorporation. Features in the measured Raman spectra of $Ge_{1-x}Sn_x$ NWs with x = 0.06 and 0.08 are consistent with the reported theoretical analysis. Polarization-dependent Raman spectroscopy further confirms different components of the Raman spectrum and also sheds light on the symmetry of the Raman components. The localized electric field at close vicinity to Sn clusters, as confirmed by simulation, activates the higher-order Raman scattering in the high-frequency Ge–Ge mode, which originates from Ge–Ge compression by the Sn clusters. This has been proved from the laser power-dependent nonlinear enhancement of the intensity of the high-frequency Ge–Ge mode. The Grüneisen parameters calculated from the temperature-dependent Raman study in the regime of 83–550 K show the evolution of an isobaric Grüneisen parameter as a function of Sn concentration. The result has important implications to understand the GeSn heterogeneous nanostructures e.g., the Ge/GeSn core–shell nanowires or a quantum well etc. A detailed characterization of Raman modes and splitting of degenerate phonon modes could be essential in understanding the lattice dynamics in these structures. The stimulated Raman scattering observed for the GeSn alloy has significant importance

Table 1 First-order temperature co-efficient for the i^{th} mode, (β_i), obtained from the temperature dependent Raman spectra, and calculated $Ge_{1-x}Sn_x$ parameter for the i^{th} mode (γ_{ip}) using eqn (4) for $Ge_{1x}Sn_x$ NWs with (a) x = 0, (b) x = 0.01, (c) x = 0.06, and (d) x = 0.08. Sn dependent values are taken from [41]

Sample	Mode	α ($\times 10^{-6}$) (K^{-1}) [from Ref.[41]]	β_i (cm^{-1} K^{-1})	γ_{ip}
x = 0	Ge-Ge	5.86	-0.01972	11.36
x = 0.01	Ge-Ge	5.84	-0.01072	6.12
x = 0.06	Ge-Ge relaxed	5.84	-0.02209	12.99
	Ge-Ge		-0.01665	9.67
	Ge-Ge compressed		-0.01681	9.68
x = 0.08	Ge-Ge relaxed	5.88	-0.02270	13.33
	Ge-Ge		-0.01927	11.20
	Ge-Ge compressed		-0.01735	9.99

to determine electric field distribution and structural disorder at the interface of complex GeSn heterogeneous nanostructures as well as other group IV semiconductor–metal alloys.

Author contributions

A.S. conceived the project. S.B., J.D. and J.D.H. prepared the sample and performed SEM and TEM analysis. S.R. performed the Raman spectroscopy experiments, analyzed the data and prepared the figures. P.K.M. performed the COMSOL Multiphysics simulation thereof with input from S.R. and A.S.. S.R., S.B. and A.S. wrote the paper with input from all the authors. All the authors have gone through the paper and commented on it.

Conflicts of interest

The authors declare no conflict of interest.

Acknowledgements

We acknowledge financial support from Science Engineering Research Board (SERB), India (File Number: EMR/2017/002107). This work was also supported by Science Foundation Ireland (SFI; project no. 14/IA/2513). The authors thank Dr. Christopher A. Broderick (Tyndall National Institute, Ireland) for useful discussions. Authors are thankful to Dr. Michele Conroy of University College London and Dr. Clive Downing of Advanced Microscopy Laboratory (AML), Trinity College, Dublin for their contribution in high-resolution microscopy and elemental mapping.

Notes and references

1 S. Gupta, B. Magyari-Kope, Y. Nishi and K. C. Saraswat, *J. Appl. Phys*, 2013, **113**, year.

2 M. R. Bauer, J. Tolle, C. Bungay, A. V. G. Chizmeshya, D. J. Smith, J. Menéndez and J. Kouvetakis, *Solid State Commun.*, 2003, **127**, 355.

3 M. Bauer, J. Taraci, J. Tolle, A. Chizmeshya, S. Zollner, D. Smith, J. Menéndez, C. Hu and J. Kouvetakis, *Appl. Phys. Lett.*, 2002, **81**, 2992.

4 S. Biswas, J. Doherty, D. Saladukha, Q. Ramasse, D. Majumdar, M. Upmanyu, A. Singha, T. Ochalski, M. A. Morris and J. D. Holmes, *Nature Commun.*, 2016, **7**, 11405.

5 E. Kasper, M. Kittler, M. Oehme and T. Arguirov, *Photonics Res.*, 2013, **1**, 69.

6 C. Hu, 2008 9th International Conference on Solid-State and Integrated-Circuit Technology, 2008, pp. 16–20.

7 M. D. Brubaker, P. T. Blanchard, J. B. Schlager, A. W. Sanders, A. Roshko, S. M. Duff, J. M. Gray, V. M. Bright, N. A. Sanford and K. A. Bertness, *Nano Lett.*, 2013, **13**, 374.

8 Z. Wang and B. Nabet, *Nanophotonics*, 2015, **4**, 491.

9 R. A. Soref, *Nature Photonics*, 2010, **4**, 495.

10 R. Chen, H. Lin, Y. Huo, C. Hitzman, T. I. Kamins and J. S. Harris, *Appl. Phys. Lett.*, 2011, **99**, 181125.

11 C. L. Senaratne, J. D. Gallagher, T. Aoki, J. Kouvetakis and J. Menéndez, *Chem. Mater.*, 2014, **26**, 6033.

12 C. M. Lieber, *MRS Bull.*, 2011, **36**, 1052.

13 M. T. Bjork, B. J. Ohlsson, T. Sass, A. I. Persson, C. Thelander, M. H. Magnusson, K. Deppert, L. R. Wallenberg and L. Samuelson, *Appl. Phys. Lett.*, 2002, **81**, 4458.

14 A. P. Alivisatos, *Science*, 1996, **271**, 933–937.

15 M. D. Kelzenberg, D. B. Turner-Evans, B. M. Kayes, M. A. Filler, M. C. Putnam, N. S. Lewis and H. A. Atwater, *Nano Lett.*, 2007, **8**, 710.

16 B. Tian, X. Zheng, T. J. Kempa, Y. Fang, N. Yu, G. Yu, J. Huang and C. M. Lieber, *Nature*, 2007, **449**, 885.

17 E. C. Garnett and P. Yang, *J. Am. Chem. Soc.*, 2008, **130**, 9224.

18 H. J. Joyce, Q. Gao, H. H. Tan, C. Jagadish, Y. Kim, J. Zou, L. M. Smith, H. E. Jackson, J. M. Yarrison-Rice, P. Parkinson and M. B. Johnston, *Prog. Quantum Electron.*, 2011, **35**, 23.

19 N.-N. Feng, D. Feng, S. Liao, X. Wang, P. Dong, H. Liang, C.-C. Kung, W. Qian, J. Fong, R. Shafiiha, Y. Luo, J. Cunningham, A. V. Krishnamoorthy and M. Asghari, *Optics Express*, 2011, **19**, 7062.

20 A. B. Greytak, C. J. Barrelet, Y. Li and C. M. Lieber, *Appl. Phys. Lett.*, 2005, **87**, 151103.

21 S. Zaima, O. Nakatsuka, N. Taoka, M. Kurosawa, W. Takeuchi and M. Sakashita, *Science and Technology of Advanced Materials*, 2015, **16**, 043502.

22 A. Sergeev, M. Y. Reizer and V. Mitin, *Phys. Rev. Lett.*, 2005, **94**, 136602.

23 J. Kierdaszuk, P. Kaźmierczak, A. Drabińska, K. Korona, A. Wołłoś, M. Kamińska, A. Wysmołłek, I. Pasternak, A. Krajewska, K. Pakułła and Z. R. Zytkiewicz, *Phys. Rev. B*, 2015, **92**, 195403.

24 K. Jeganathan, R. K. Debnath, R. Meijers, T. Stoica, R. Calarco, D. Grützmacher and H. Lüth, *J. Appl. Phys.*, 2009, **105**, 123707.

25 P. Luo, F. Zhuge, Q. Zhang, Y. Chen, L. Lv, Y. Huang, H. Li and T. Zhai, *Nanoscale Horiz.*, 2019, **4**, 26.

26 S. Parida, A. Patsha, S. Bera and S. Dhara, *J. Phys. D: Appl. Phys.*, 2017, **50**, 275103.

27 M. Šćepanović, M. Grujić-Brojčin, K. Vojisavljević and T. Srećković, *J. Appl. Phys.*, 2011, **109**, 034313.

28 K. Alberi and M. A. Scarpulla, *J. Appl. Phys.*, 2018, **123**, 185702.

29 X. Z. Yu, Y. Yang, W. Pan and W. Z. Shen, *Appl. Phys. Lett.*, 2008, **92**, 092106.

30 N. E. Massa, J. A. Alonso, M. J. Martínez-Lope and M. T. Casais, *Phys. Rev. B*, 2005, **72**, 214303.

31 J. Doherty, S. Biswas, D. McNulty, C. Downing, S. Raha, C. O'Regan, A. Singha, C. O'Dwyer and J. D. Holmes, *Chem. Mater.*, 2019, **31**, 4016.

32 J. Doherty, S. Biswas, D. Saladukha, Q. Ramasse, T. S. Bhattacharya, A. Singha, T. J. Ochalski and J. D. Holmes, *J. Mater. Chem. C*, 2018, **6**, 8738.

33 S. F. Li, M. R. Bauer, J. Menéndez and J. Kouvetakis, *Appl. Phys. Lett.*, 2004, **84**, 867.

34 D. S. P. Tanner, S. Raha, J. Doherty, S. Biswas, J. D. Holmes, E. P. O'Reilly, A. Singha and C. A. Broderick, *Raman spectroscopy of group-IV $Ge_{1-x}Sn_x$ alloys: theory and experiment*, 2021, `https://arxiv.org/abs/2112.00523`.

35 C. Fasolato, M. D. Luca, D. Djomani, L. Vincent, C. Renard, G. D. Iorio, V. Paillard, M. Amato, R. Rurali and I. Zardo, *Nano Lett.*, 2018, **18**, 7075–7084.

36 D. de Matteis, M. De Luca, E. M. T. Fadaly, M. A. Verheijen, M. López-Suárez, R. Rurali, E. P. A. M. Bakkers and I. Zardo, *ACS Nano*, 2020, **14**, 6845–6856.

37 P. H. Tan, K. Brunner, D. Bougeard and G. Abstreiter, *Phys. Rev. B*, 2003, **68**, 125302.

38 S. Jiang, Y. Zhang, R. Zhang, C. Hu, M. Liao, Y. Luo, J. Yang and Z. Dong, *Nature Nanotechnology*, 2015, **10**, 865.

39 P. Kukura, D. W. McCamant and R. A. Mathies, *Annu. Rev. Phys. Chem.*, 2007, **58**, 461.

40 W. Min, C. W. Freudiger, S. Lu and X. S. Xie, *Annu. Rev. Phys. Chem.*, 2011, **62**, 507.

41 R. Roucka, Y.-Y. Fang, J. Kouvetakis, A. V. G. Chizmeshya and J. Menéndez, *Phys. Rev. B*, 2010, **81**, 245214.

42 S. Sahoo, A. P. S. Gaur, M. Ahmadi, M. J.-F. Guinel and R. S. Katiyar, *The Journal of Physical Chemistry C*, 2013, **117**, 9042–9047.

43 S. Sett, V. K. Aggarwal, A. Singha and A. K. Raychaudhuri, *Phys. Rev. Applied*, 2020, **13**, 054008.

44 M. Balkanski, R. F. Wallis and E. Haro, *Phys. Rev. B*, 1983, **28**, 1928.

45 J. Y. Cho, X. Shi, J. R. Salvador, G. P. Meisner, J. Yang, H. Wang, A. A. Wereszczak, X. Zhou and C. Uher, *Phys. Rev. B*, 2011, **84**, 085207.

46 S. Raha, D. Srivastava, S. Biswas, G.-G. Adria, A. J. Karttunen, J. D. Holmes and A. Singha, *Appl. Phys. Lett.*, 2021, **119**, 232105.